

Provided for non-commercial research and education use.
Not for reproduction, distribution or commercial use.



This article was published in an Elsevier journal. The attached copy is furnished to the author for non-commercial research and education use, including for instruction at the author's institution, sharing with colleagues and providing to institution administration.

Other uses, including reproduction and distribution, or selling or licensing copies, or posting to personal, institutional or third party websites are prohibited.

In most cases authors are permitted to post their version of the article (e.g. in Word or Tex form) to their personal website or institutional repository. Authors requiring further information regarding Elsevier's archiving and manuscript policies are encouraged to visit:

<http://www.elsevier.com/copyright>



Internal structure of clusters of partially coherent nanocrystallites in Cr–Al–N and Cr–Al–Si–N coatings

David Rafaja^{a,*}, Christina Wüstefeld^a, Milan Dopita^{a,b}, Milan Růžička^c,
Volker Klemm^a, Gerhard Schreiber^a, Dietrich Heger^a, Michal Šíma^c

^a Institute of Materials Science, TU Bergakademie Freiberg, Gustav-Zeuner-Str. 5, D-09599 Freiberg, Germany

^b Department of Condensed Matter Physics, Faculty of Mathematics and Physics,
Charles University, Ke Karlovu 5, CZ-121 16 Prague, Czech Republic

^c SHM Ltd., Průmyslová 3, CZ-787 01 Šumperk, Czech Republic

Received 23 February 2007; accepted in revised form 2 April 2007

Available online 11 April 2007

Abstract

Nano-sized clusters consisting of strongly preferentially oriented, partially coherent nanocrystallites were observed in Cr–Al–N and Cr–Al–Si–N coatings deposited using cathodic arc evaporation. Microstructure analysis of the coatings, which was done using the combination of X-ray diffraction (XRD) and transmission electron microscopy with high resolution (HRTEM), revealed furthermore stress-free lattice parameters, size and local disorientation of crystallites within the nano-sized clusters in dependence on the aluminium and silicon contents, mean size of these clusters and the kind of structure defects. Within the face-centred cubic (fcc) $\text{Cr}_{1-x-y}\text{Al}_x\text{Si}_y\text{N}$ phase, the stress-free lattice parameter was described by the equation $a = (0.41486 - 0.00827 \cdot x + 0.034 \cdot y)$ nm. The size of individual crystallites decreased from ~ 11 nm in $\text{Cr}_{0.92}\text{Al}_{0.08}\text{N}$ to ~ 4 nm in $\text{Cr}_{0.24}\text{Al}_{0.65}\text{Si}_{0.10}\text{N}$. These nanocrystallites formed clusters with the mean size between 36 and 56 nm. The mutual disorientation of the partially coherent nanocrystallites forming the clusters increased with increasing aluminium and silicon contents from 0.5° to several degrees. The disorientation of neighbouring nanocrystallites was explained by the presence of screw dislocations and by presence of phase interfaces in coatings containing a single fcc phase and several phases, respectively.

© 2007 Elsevier B.V. All rights reserved.

Keywords: Cathodic arc evaporation; Nanocomposite; Partially coherent crystallites; Screw dislocations; XRD; HRTEM

1. Introduction

The relationship between the microstructure and properties of nanocrystalline coatings or thin film nanocomposites, which are based on nitrides of transition metals, is the main topic of many studies. This is also true for chromium nitride coatings, which contain additionally aluminium and silicon. The Cr–Al–N and Cr–Al–Si–N coatings are used with benefit in special industrial applications, e.g. for punching of perforated sheets [1], as super-elastic coatings for high end spindle bearings [2] or as thermal barriers redirecting the heat from the cutting tool into the chip [3]. In these applications, the microstructure and properties of the Cr–Al–N and Cr–Al–Si–N coatings are frequently tailored

by varying their chemical composition that influences primarily their phase composition [4–7]. For prediction of the phase composition in transition metal aluminium nitrides, Makino [6] published a theoretical approach that uses the band parameters method, which is based on the concept of the localized electron theory. For the face-centred cubic (fcc) $\text{Cr}_{1-x}\text{Al}_x\text{N}$, this approach yielded the maximum aluminium contents of $x = 0.772$. Experiments performed on the Cr–Al–N coatings deposited using magnetron sputtering [4] yielded the maximum aluminium contents between $x = 0.67$ and 0.75 . Cr–Al–N coatings deposited using rf-assisted magnetron sputtering [5] were composed of the single fcc phase up to $x = 0.7$ – 0.8 . The second phase, which forms above the solubility limit of aluminium in fcc $\text{Cr}_{1-x}\text{Al}_x\text{N}$, is AlN with the wurtzite crystal structure. Many applications of the CrN and Cr–Al–N coatings exploit their high oxidation resistance [3,8]. The onset of the oxidation in CrN is typically above 700°C ; the exact temperature of the beginning oxidation

* Corresponding author. Tel.: +49 3731 39 2299; fax: +49 3731 39 3657.
E-mail address: Rafaja@ww.tu-freiberg.de (D. Rafaja).

depends on the microstructure of the coatings [8]. Increasing aluminium contents improves the oxidation resistance of fcc (Cr, Al) N [9–12]. Reiter et al. [11] observed the onset of a rapid oxidation above 950 °C and 1000 °C for coatings with the chemical compositions Cr_{0.79}Al_{0.21}N and Cr_{0.54}Al_{0.46}N, respectively.

As for other nanocomposites [13–15], the crystallite size and the morphology of the internal interfaces are the most important factors influencing the mechanical properties of Cr–Al–N and Cr–Al–Si–N nanocomposites. This is true particularly for their hardness, as the high hardness in nanocomposites is usually explained by a high elastic recovery of the material and by a high resistance against crack formation [16] or by prevention of the grain boundary sliding [17,18]. The relationship between crystallite size in stoichiometric CrN coatings and their hardness was described in detail by Mayrhofer et al. in [19], who has shown that the hardness of CrN coatings obeys the Hall–Petch relationship up to approximately 15 nm. In smaller crystallites, the hardness decreased. Like in the Ti–Al–Si–N system, the addition of silicon into Cr–Al–N improves the hardness of the nanocomposites. Approximately 9 at.% of Si was regarded as an optimum silicon concentration that increased the hardness of CrN from ~23 GPa to ~35 GPa and the hardness of Cr–Al–N from ~25 GPa to ~55 GPa [20]. Frequently, nanocomposites form during a decomposition process [6,21–28], which is anticipated to be accelerated by the presence of silicon, particularly in the Ti–Al–Si–N system. It was verified by first-principle calculations [29,30] that in Ti–Si–N the neighbouring TiN nanocrystallites can be connected by a slab of silicon nitride. An analogous inter-connection of neighbouring nanocrystallites of fcc-(Ti, Al) N and hexagonal AlN having similar inter-planar spacings was observed experimentally in Ti–Al–Si–N nanocomposites [31]. Such an inter-connection or inter-twinning of nanocrystallites was anticipated to be responsible for formation of local intrinsic stresses at the crystallites boundaries and thus for an additional increase of the hardness in these nanocomposites.

A very important experimental tool in description of the inter-twinning of neighbouring crystallites was the effect of the partial crystallographic coherence [32], which was exploited to determine small mutual disorientations of nanocrystallites. As discussed in [32], partially coherent nanocrystallites produce broad reciprocal lattice points. The size of the reciprocal lattice points that is related to the broadening of X-ray diffraction lines is reciprocally proportional to the crystallite size. Broad reciprocal lattice points overlap partially each other at small disorientations of the neighbouring crystallites. The overlap of the reciprocal lattice points from neighbouring crystallites is perfect at the origin of the reciprocal space, where the size of the diffraction vector

$$q = \frac{4\pi}{\lambda} \sin \theta \quad (1)$$

is equal to zero. With increasing length of the diffraction vector, the overlap of the reciprocal lattice points decreases until it disappears [31]. In Eq. (1), λ is the wavelength of X-rays and θ the diffraction angle. The partial overlap of the reciprocal lattice points corresponds to the coherence of X-rays scattered by the

related crystallites, thus it causes a “narrowing” of the broad diffraction lines from nanocrystallites (or it reduces the line broadening in nanocrystallites). An interpretation of this effect in the direct space is that the X-ray scattering cannot distinguish the partially coherent crystallites from each other. Therefore, partially coherent crystallites appear consequently larger than they are in a diffraction experiment. The apparent size of the crystallites varies with the size of the diffraction vector because the overlap of the reciprocal lattice points and the remaining XRD line broadening vary with the size of the diffraction vector. From the dependence of the diffraction line broadening on the size of the diffraction vector, two limiting quantities related to the apparent size of the crystallites can be calculated and assigned to the microstructure features, which can be verified by transmission electron microscopy (TEM): the size of individual nanocrystallites [32] and the size of clusters, which are composed of these nanocrystallites [33]. A requirement for the partial coherence of crystallites is that they have a similar crystallographic orientation. The maximum disorientation of partially coherent nanocrystallites is about 1° for the crystallite size of approximately 10 nm. Some examples are given in Section 3.

In this contribution, the phenomenon of the partial coherence of crystallites is employed to determine the size of clusters of partially coherent nanocrystallites, the average size of the nanocrystallites and their mutual disorientation in Cr–Al–N and Cr–Al–Si–N coatings containing a single phase or several phases, which are important parameters and features that can be used for a quantitative description of the microstructure of the coatings. In coatings containing several phases, the above features were used to describe quantitatively the microstructure of the coatings in terms of the models, which were derived or used, for instance, in Refs. [13–16,22,31,34–38]. These microstructure models assume the presence of at least two phases in the coatings and describe spatial distribution of the phases and/or the atomic ordering at the interfaces between different phases. In Cr–Al–N coatings containing a single phase, in which the same microstructure features were found like in the samples containing several phases, i.e. the clusters of partially coherent crystallites, the formation of these clusters was explained by the development of screw dislocations that were observed using TEM.

2. Experimental details

The Cr–Al–N and Cr–Al–Si–N coatings were deposited using cathodic arc evaporation (CAE) in nitrogen atmosphere at the working pressure of 1.3 Pa from two laterally rotating arc cathodes (π -80 from PLATIT) [39]. One cathode was made of chromium, the second one either from pure aluminium (for deposition of the Cr–Al–N coatings) or from aluminium containing 11 at.% Si (for deposition of the Cr–Al–Si–N coatings). The ion current on the Cr cathode was 80 A, the ion current on the Al or Al–Si cathode 120 A. The bias voltage was –75 V in all cases. Polished plates of cemented carbide were used as substrates. The base pressure was 5×10^{-3} Pa, the deposition temperature approximately 450 °C. In order to obtain a series of samples with a variable [Cr]/[Al] or [Cr]/([Al]+[Si]) ratio in one deposition run, the positions of individual samples

did not change during the deposition process, i.e. the samples were not rotated unlike in technical deposition processes. The distance between the respective cathode and the respective substrate defined the chemical composition of individual coatings as discussed in Refs. [7,40].

The chemical composition of the Cr–Al–N and Cr–Al–Si–N coatings was determined using the electron probe microanalysis with wavelength-dispersive spectroscopy of characteristic X-rays (EPMA/WDS). Energy of the primary electrons in EPMA was 12 keV. High-purity Cr, Al and Si (99.999 %) were used as calibration standards together with BN, Fe₂N and Fe₄N. The stoichiometry ratios in individual samples are given in Tables 1 and 2 as averaged over 40 points measured across each sample. The maximum difference in the concentration of the analysed elements, i.e. Cr, Al, Si and N, within the individual samples was 2 at.%. The nitrogen contents was (54±3) at.% in all samples under study, which can be regarded as 50 at.% within the statistical spread in the experimental data. The stoichiometric composition of the samples regarding the nitrogen concentration was anticipated as based on the phase diagram of the Cr–N system [41] and confirmed by the electron probe microanalysis done on the Cr–Si–N thin films in [42]. The oxygen contents in the samples were below 0.1 at.% as discussed in [7]. Although aluminium and silicon were deposited from the same cathode, the [Si]/[Al] ratio in the coatings increased with decreasing chromium contents, i.e. with decreasing distance between the Al–Si cathode and the substrates in this deposition geometry. The hardness of the coatings, which is listed in Tables 1 and 2, was calculated from the indentation load–displacement curve [43] measured in 10 points per sample using a computer-controlled Fischerscope H100 microhardness tester. The maximum load of 70 mN, which was recommended for super-hard coatings in [44], was reached in 20 s. The unloading time was 20 s as well. The maximum indentation depth ranged between 0.3 and 0.4 μm, which are below 10% of the thickness in most coatings (compare thickness of the coatings given in Tables 1 and 2). The systematic variation of the thickness is caused by different distances between the cathodes and the substrates, which influences, besides the chemical composition, also the growth rate.

Phase composition of the coatings, stress-free lattice parameters, size of crystallites, size of clusters of partially coherent crystallites and the mutual disorientation of the partially coherent crystallites in the clusters were concluded from X-ray diffraction experiments that were performed in the glancing-angle X-ray

Table 1
Chemical composition, thickness and hardness of the Cr–Al–N coatings

Chemical composition	Thickness [μm]	Hardness [GPa]
Cr _{0.92(3)} Al _{0.08(1)} N	3.3±0.1	23.1±1.4
Cr _{0.83(3)} Al _{0.17(2)} N	5.0±0.1	25.7±1.4
Cr _{0.75(3)} Al _{0.25(3)} N	5.6±0.1	28.0±1.2
Cr _{0.54(3)} Al _{0.46(2)} N	7.2±0.1	36.3±1.4
Cr _{0.46(3)} Al _{0.54(2)} N	6.3±0.1	38.1±1.8
Cr _{0.30(2)} Al _{0.70(3)} N	5.4±0.1	38.3±1.7
Cr _{0.08(1)} Al _{0.91(3)} N	4.4±0.1	31.6±1.2

Table 2

Chemical composition, the [Si]/([Al]+[Si]) ratio, thickness and hardness of the Cr–Al–Si–N coatings

Chemical composition	[Si]/([Al]+[Si])	Thickness[μm]	Hardness [GPa]
Cr _{0.91(2)} Al _{0.08(1)} Si _{0.007(1)} N	(8.1±1.5) %	4.5±0.2	27.7±0.7
Cr _{0.84(3)} Al _{0.15(2)} Si _{0.013(3)} N	(8.1±2.1) %	6.3±0.2	29.6±1.2
Cr _{0.69(3)} Al _{0.28(3)} Si _{0.027(4)} N	(8.6±1.6) %	7.9±0.3	34.4±1.6
Cr _{0.52(3)} Al _{0.43(2)} Si _{0.049(3)} N	(10.1±0.8) %	8.7±0.3	41.5±0.5
Cr _{0.40(3)} Al _{0.52(3)} Si _{0.077(6)} N	(12.9±1.3) %	8.6±0.3	44.5±1.7
Cr _{0.24(2)} Al _{0.65(2)} Si _{0.102(8)} N	(13.5±1.2) %	7.5±0.3	39.1±1.3
Cr _{0.07(1)} Al _{0.81(3)} Si _{0.118(7)} N	(12.7±0.9) %	3.6±0.2	34.9±0.7

diffraction (GAXRD) geometry on a D8 diffractometer from Bruker AXS. In these diffraction experiments, copper radiation from a sealed X-ray tube was reflected by a parabolic Goebel mirror and directed to the sample surface. The angle of incidence was kept constant at 3°. Diffracted radiation was registered by a scintillation detector, which was preceded by a Soller collimator with the acceptance of 0.12° and by a flat LiF monochromator. The LiF monochromator located in the front of the detector changed the $K_{\alpha 2}/K_{\alpha 1}$ intensity ratio to 0.08. Additional measurements of the stress-free lattice parameter using the $\sin^2\psi$ method were carried out with an Eulerian cradle mounted on a PTS diffractometer from Seifert. High-resolution transmission electron microscopy (HRTEM) was done on a 200 kV analytical high-resolution transmission electron microscope JEM 2010 FEF from Jeol equipped by ultra-high-resolution objective lens ($C_s=0.5$ mm) and in-column energy filter. The latter was used to select only the elastic electrons for the HRTEM image formation. The analysis of the dislocation structures was performed using the diffraction contrast in the bright field image. The specimens for TEM were prepared in the plane-view orientation, which is more convenient for a direct comparison of the XRD and HRTEM results. The coatings were first removed from the substrates, mechanically pre-thinned and etched by ion beam. The final step in the specimen preparation was a plasma cleaning procedure.

3. Experimental results

3.1. Phase stability and lattice parameters

Diffraction patterns of the Cr_{1-x}Al_xN and Cr_{1-x-y}Al_xSi_yN coatings shown in Figs. 1 and 2 confirmed that samples with the higher chromium contents than Cr_{0.46}Al_{0.54}N and Cr_{0.40}Al_{0.52}Si_{0.08}N, respectively, contain only one fcc phase. In samples with a lower chromium contents, wurtzitic AlN was identified as a second crystalline phase in the coatings. The third phase found in the XRD patterns was tungsten carbide from the substrate. Positions of the diffraction lines are marked in Figs. 1 and 2 for individual phases. The positions of the diffraction lines from the cubic phases, i.e. Cr_{1-x}Al_xN and Cr_{1-x-y}Al_xSi_yN, shift with the chemical composition of the samples that is due to the dependence of the lattice parameter on the stoichiometry in both systems. Because of the strong anisotropy of the elastic constants in the Cr–Al–N and Cr–Al–Si–N systems, the stress-free lattice parameters given in Fig. 3 were calculated using the

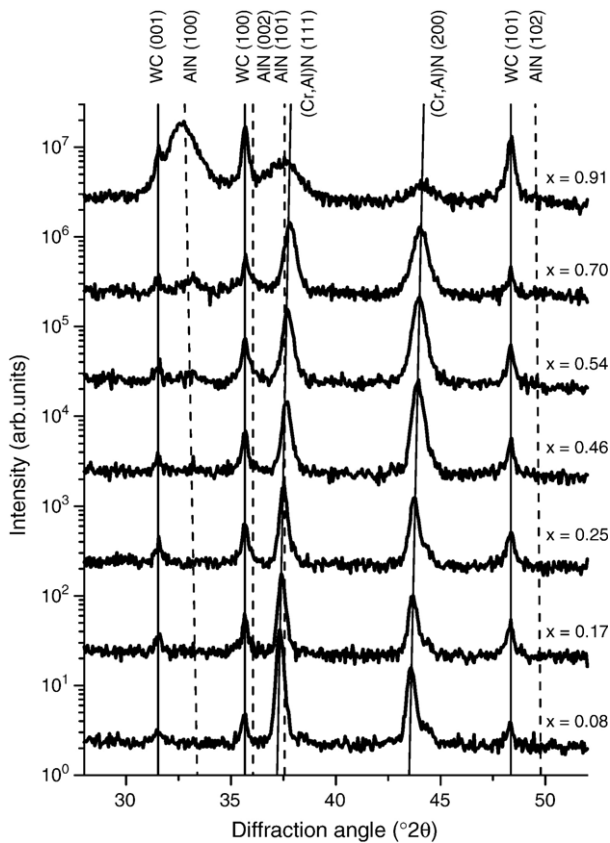


Fig. 1. Parts of the diffraction patterns of the $\text{Cr}_{1-x}\text{Al}_x\text{N}$ coatings with different chemical compositions. The vertical lines indicate the positions of individual XRD lines. Individual diffraction patterns were mutually shifted for clarity.

routine described in Ref. [7], which takes the well-known dependence of the elastic constants, e.g. [45–48], on the orientation factor

$$\Gamma = \frac{h^2k^2 + k^2\ell^2 + \ell^2h^2}{(h^2 + k^2 + \ell^2)^2} \quad (2)$$

into account. Results of this calculation were verified using the $\sin^2\psi$ method [49] applied on the lattice parameter a_{200} , for which is $\Gamma=0$. Dependence of the stress-free lattice parameters obtained from the XRD measurements on the chemical composition of the samples obtained using EPMA/WDX is shown by filled symbols in Fig. 3. Stress-free lattice parameter of CrN, i.e. for $[\text{Cr}]/([\text{Cr}]+[\text{Al}]+[\text{Si}])=1$, was taken from the ICSD database [50]. Solid lines connect lattice parameters that were calculated from the function:

$$a = [0.41486(2) - 0.00827(1) \cdot x + 0.034(1) \cdot y] \text{nm} \quad (3)$$

for the chemical compositions of individual samples. The parameters x and y have the meaning of the stoichiometry ratios of aluminium and silicon in the fcc phase of $\text{Cr}_{1-x-y}\text{Al}_x\text{Si}_y\text{N}$. The numerical values in Eq. (3) were obtained from the linear regression that was done for the four chromium-richest samples in each series, which were found to contain a single crystalline phase. The first numerical coefficient in Eq. (3) has the meaning

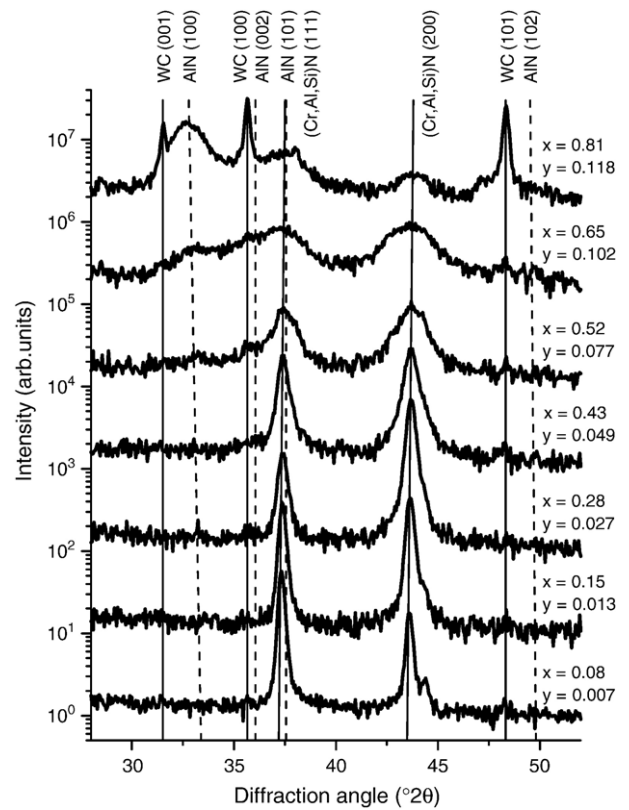


Fig. 2. Parts of the diffraction patterns of the $\text{Cr}_{1-x-y}\text{Al}_x\text{Si}_y\text{N}$ coatings with different chemical compositions. The vertical lines indicate the positions of individual XRD lines. Individual diffraction patterns were mutually shifted for clarity.

of the intrinsic lattice parameter of CrN. The second numerical coefficient quantifies the decrease of the lattice parameter in fcc Cr–Al–Si–N with increasing aluminium contents, the third one the increase of the lattice parameter with increasing silicon contents. Estimated standard deviations of the coefficients are given in parenthesis in Eq. (3).

The good match between the stress-free lattice parameters measured in chromium-rich samples up to $\text{Cr}_{0.54}\text{Al}_{0.46}\text{N}$ or

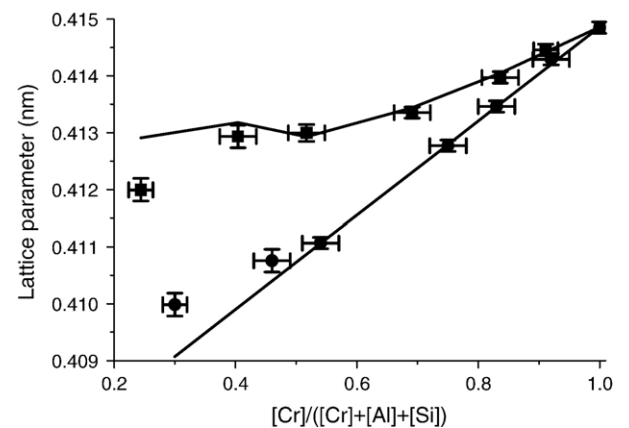


Fig. 3. Dependence of the stress-free lattice parameters on the chemical composition of the Cr–Al–N (●) and Cr–Al–Si–N (■) coatings. The solid lines show lattice parameters calculated according to Eq. (3).

$\text{Cr}_{0.52}\text{Al}_{0.43}\text{Si}_{0.05}\text{N}$ and the stress-free lattice parameters calculated using Eq. (3) confirmed the result of the XRD phase analysis that the samples contain a single fcc phase in this concentration range. At higher aluminium contents in the Cr–Al–N coatings, the measured stress-free lattice parameter of the fcc phase is larger than the calculated lattice parameters (Fig. 3). The reason is the segregation of aluminium from the host fcc crystal structure, which led to the development of AlN as observed by XRD phase analysis. In the Cr–Al–Si–N system, both Al and Si segregated from the host structure at lower chromium contents than $\text{Cr}_{0.52}\text{Al}_{0.43}\text{Si}_{0.05}\text{N}$. Segregation of aluminium was confirmed by XRD phase analysis, which recognized wurtzitic AlN. As it follows from Eq. (3), the increase of the stress-free lattice parameter with increasing silicon contents is larger than its decrease with increasing aluminium contents. Accordingly, the stress-free lattice parameter measured in the samples $\text{Cr}_{0.40}\text{Al}_{0.52}\text{Si}_{0.08}\text{N}$ and $\text{Cr}_{0.24}\text{Al}_{0.65}\text{Si}_{0.10}\text{N}$ is smaller than the value calculated from Eq. (3). Segregation of aluminium and silicon from the host structure of the fcc chromium nitride leads to the development of the nanocomposite microstructure as discussed below that is well-known to enhance the hardness of the coatings, see e.g. [13,14]. The highest hardness was observed in the Cr–Al–N and Cr–Al–Si–N coatings, in which the onset of AlN was found (see Tables 1 and 2). Increasing amount of the wurtzitic AlN caused a decrease of the hardness in both systems, Cr–Al–N and Cr–Al–Si–N. In the Cr–Al–N coatings, the maximum hardness correlates with the minimum crystallite size. In the Cr–Al–Si–N coatings, the maximum hardness was observed at the crystallite size of 4.5 nm. These results, particularly the correlation between the maximum of the hardness and the onset of the segregation of the AlN, confirm the hypothesis that the intrinsic stresses at the crystallites boundaries can additionally enhance the hardness.

3.2. Clusters of partially coherent crystallites

Size of individual crystallites, their mutual disorientation and the size of clusters consisting of partially coherent crystallites were obtained from the XRD line broadening [7,31–33] and verified by TEM and HRTEM. An example of the dependence of the XRD line broadening on sinus of the diffraction angle, $\sin \theta$, which is according to Eq. (1) proportional to the size of the diffraction vector, is shown in Fig. 4 for $\text{Cr}_{0.92}\text{Al}_{0.08}\text{N}$. As shown in [32], the saturated line broadening (for $\sin \theta > 0.75$ in Fig. 4) reveals the reciprocal crystallite size like the classical Scherrer equation or the Williamson–Hall approach [51] at zero microstrain. In the region of the diffraction angles, where the crystallites are partially coherent, the effect of the partial coherence of nanocrystallites causes a successive reduction of the XRD line broadening with decreasing diffraction angle [32]. Diffraction angle for which the effect of the partial coherence of nanocrystallites onsets depends on the mutual disorientation of partially coherent crystallites [7,32,33]. The smaller the mutual disorientation of crystallites, the higher is the diffraction angle, for which the crystallites are still partially coherent. For $\text{Cr}_{0.92}\text{Al}_{0.08}\text{N}$ (Fig. 4), the calculated mutual disorientation of partially

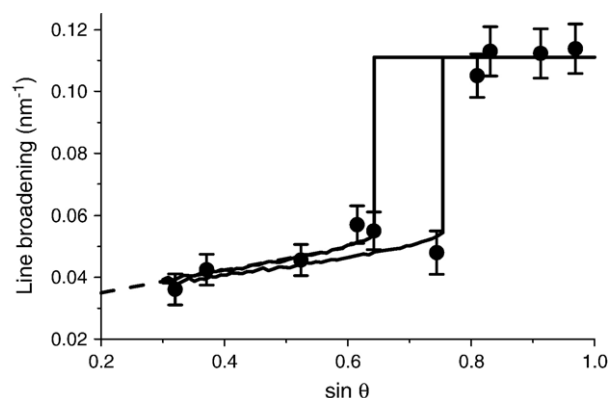


Fig. 4. Dependence of the XRD line broadening on $\sin \theta$ as measured for the $\text{Cr}_{0.92}\text{Al}_{0.08}\text{N}$ coating. The steep increase of the line broadening between $\sin \theta = 0.65$ and 0.75 indicates extinction of the partial coherence of crystallites. The solid lines show the XRD line broadening that was calculated according to [32] for two partially coherent crystallites having the size of 11 nm and the disorientation of 0.50° (lower curve) and 0.56° (upper curve) in each cluster. The dashed line shows extrapolation of the XRD line broadening in the partially coherent region to $q=0$.

coherent crystallites ranged between 0.50° (right-hand line) and 0.56° (left-hand line).

The size of crystallites and their mutual disorientations are plotted for individual samples in Figs. 5 and 6, respectively, as functions of the overall chemical composition. In the Cr–Al–N system, the increasing aluminium contents in the single fcc phase (up to $\text{Cr}_{0.54}\text{Al}_{0.46}\text{N}$) caused a moderate reduction of the crystallite size (solid circles in Fig. 5). Larger reduction of the crystallite size was observed in the samples, in which wurtzitic AlN developed. The mutual disorientation of neighbouring crystallites (solid circles in Fig. 6) increased slightly with increasing aluminium contents. The addition of silicon caused a further reduction of the crystallite size in comparison with the Cr–Al–N system; see solid boxes in Fig. 5. The decrease of the crystallite size with increasing aluminium and silicon contents could be described by a smooth function in contrast to the Cr–Al–N system. For low aluminium and silicon contents, the mutual disorientation of neighbouring crystallites in the Cr–Al–Si–N coatings followed the dependence found in the Cr–Al–N coatings. However, starting with $\text{Cr}_{0.52}\text{Al}_{0.43}\text{Si}_{0.05}\text{N}$ the disorientation of crystallites began to grow significantly with increasing silicon (and aluminium) contents. In $\text{Cr}_{0.40}\text{Al}_{0.52}\text{Si}_{0.08}\text{N}$, the disorientation of crystallites exceeded 1.4° , which is the maximum disorientation, for which the partial coherence of crystallites with the size of approximately 10 nm still could be observed. Such a loss of the partial crystallographic coherence of crystallites with increasing silicon contents was also observed in the Ti–Al–Si–N coatings [31], in which this phenomenon was related to the development of the amorphous Si_3N_4 phase.

A further microstructure parameter that was obtained from the XRD line broadening is the size of clusters, which consist of the partially coherent crystallites. As shown in the theory of XRD line broadening [52], the extrapolation of the XRD line width to the origin of the reciprocal space ($q=0$) yields the size of

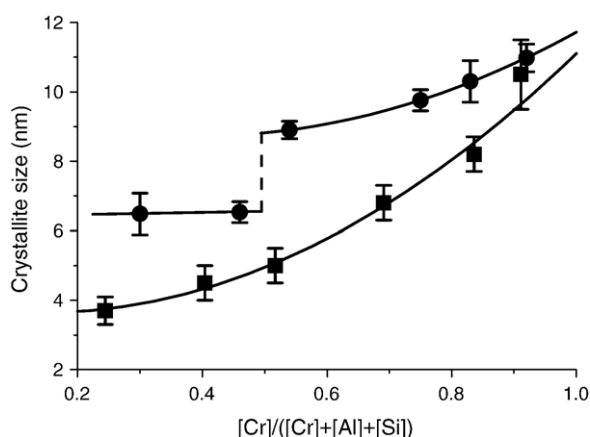


Fig. 5. Dependence of the crystallite size on the chemical composition in the Cr–Al–N (●) and Cr–Al–Si–N (■) coatings. The lines are guides for the eye.

coherently diffracting domains disregard their internal structure. In [32], it was shown that the coherence of partially coherent crystallites is enhanced at smaller diffraction vectors until the full coherence is reached at $q=0$. Thus for partially coherent crystallites, the extrapolation of the XRD line width to the origin of the reciprocal space should yield the size of clusters consisting of partially coherent crystallites instead of the size of individual crystallites. This hypothesis was confirmed by comparison of the results obtained from XRD and HRTEM. In the sample $\text{Cr}_{0.92}\text{Al}_{0.08}\text{N}$, the extrapolation of the XRD line broadening to $q=0$ (dashed line in Fig. 4) revealed that the size of clusters consisting of partially coherent crystallites is (36 ± 10) nm, which agrees well with their size obtained using HRTEM (compare with Fig. 7 for this particular sample). The low accuracy of the size of the clusters calculated from the extrapolation of the XRD line broadening is due to the fact that only the broadening of the diffraction lines affected by the partial coherence can be used for extrapolation. For this particular sample, just six diffraction lines were affected by the partial coherence. Size of the clusters consisting of partially coherent crystallites as obtained from the

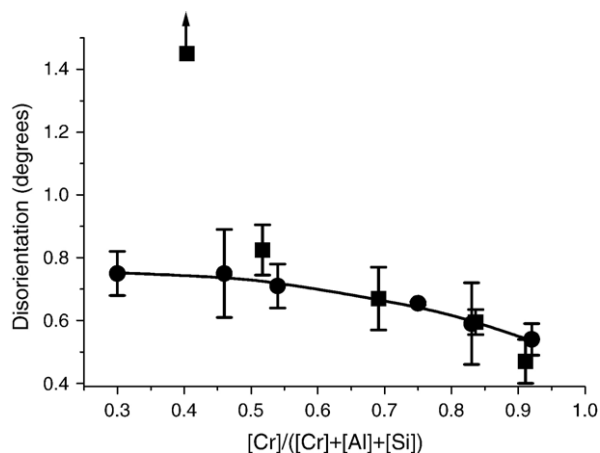


Fig. 6. Dependence of the mutual disorientation of partially coherent nanocrystallites on the chemical composition of the Cr–Al–N (●) and Cr–Al–Si–N (■) coatings. The solid line is guide for the eye.

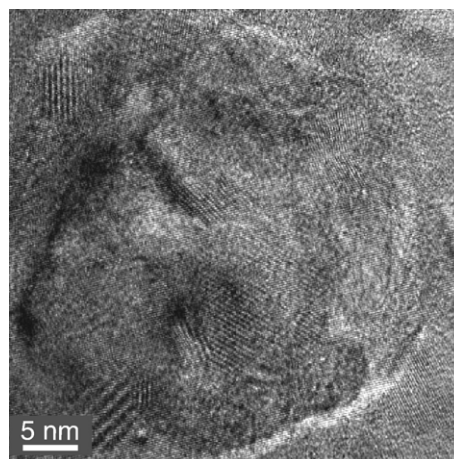


Fig. 7. HRTEM micrograph of the sample $\text{Cr}_{0.92}\text{Al}_{0.08}\text{N}$ showing a cluster consisting of partially coherent crystallites.

XRD line broadening in all samples under study ranged between 36 and 56 nm. Within the experimental accuracy, no systematic dependence of the cluster size on the chemical composition of the coatings was found.

3.3. Dislocation structures in the single-phase Cr–Al–N coatings

Small disorientations of neighbouring crystallites in nanocomposites, i.e. in materials containing more than one nano-sized phase, can be explained by the misfit of inter-atomic distances at the interfaces between individual phases [29–31]. Such an explanation of the crystallite's disorientation is applicable also for the aluminium- and silicon-rich Cr–Al–N and Cr–Al–Si–N coatings containing at least two phases as it can be seen from the steep increase of the disorientation of neighbouring crystallites in $\text{Cr}_{0.52}\text{Al}_{0.43}\text{Si}_{0.05}\text{N}$ and $\text{Cr}_{0.40}\text{Al}_{0.52}\text{Si}_{0.08}\text{N}$ (Fig. 6), where aluminium and silicon are leaving the host structure of chromium nitride (see Section 3.1 and Fig. 3). However, small disorientations of partially coherent neighbouring crystallites were also observed in the Cr–Al–N and Cr–Al–Si–N coatings with high chromium contents, which contained a single fcc phase. The fcc phase grew in clusters having the size between 36 and 56 nm as discussed in the previous section. The clusters in the single-phase coatings were composed from partially coherent crystallites having the size between 11 and 5 nm.

In analogy with the microstructure models used for description of the real structure in metallic materials and semiconductors, a possible explanation of the small disorientations of neighbouring crystallites in single-phase coatings is their disorientation due to dislocation structures. In materials containing complex dislocation structures, frequently defect-poor crystallites are observed that are separated by dislocation walls. In metallic materials, such a microstructure is usually described by Mughrabi's composite model [53]. Examples of analogous microstructural models can also be found in Refs. [54,55]. The disorientation of neighbouring crystallites that are separated by

a dislocation wall can be determined from the general formula given by Frank [56]:

$$\vec{B} = 2(\vec{r} \times \vec{\ell}) \sin \frac{\alpha}{2}, \quad (4)$$

where \vec{B} is the sum of Burgers vectors of the dislocations that are intersected by a vector \vec{r} , which lies in the dislocation wall. $\vec{\ell}$ is a unit vector, which also lies in the dislocation wall and is parallel to the tilt axis of the neighbouring crystallites. α is the disorientation of the crystallites. If the dislocation wall consists of pure edge dislocations, the tilt axis is located within the so-called tilt boundary; for dislocation walls containing only screw dislocations, the tilt axis is perpendicular to the so-called twist boundary [57].

An example of a dislocation wall in the sample $\text{Cr}_{0.92}\text{Al}_{0.08}\text{N}$ is shown in Fig. 8; the micrograph was taken in the two-beam diffraction condition [58]. In this particular case, the primary beam was parallel with the dislocation wall, which was perpendicular to the diffraction vector ($2\bar{2}0$). As the diffraction contrast does not change significantly in the neighbourhood of the dislocation wall, the sum of the Burgers vectors in the dislocation wall must be perpendicular to the diffraction vector, i.e. $\vec{q} \cdot \vec{B} = 0$. This means that the Burgers vector lies in the dislocation wall and that the tilt axis of neighbouring crystallites is perpendicular to the Burgers vector. The latter indicates that the excess dislocation of this dislocation wall is a screw dislocation. As the diffraction vector was ($2\bar{2}0$), the remaining dislocation resulting from the sum of the Burgers vectors of dislocations from the dislocation wall could be a complete screw dislocation with the Burgers vector $a/2 \langle 110 \rangle$, where a is the lattice parameter. In Fig. 9, the dislocation wall was slanted from the optical axis of the microscope, i.e. it was not parallel with the primary beam. Therefore the diffraction vector, which was ($\bar{2}42$) in this particular case, was not perpendicular to the Burgers vector of the dislocations; the dislocations become visible and their mutual distances can be estimated. Assuming that the dislocation wall is built from complete screw dislocations with the Burgers

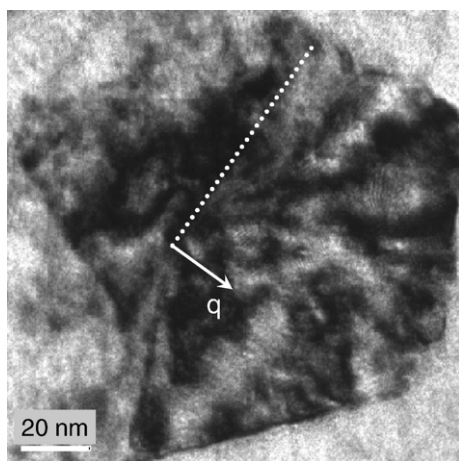


Fig. 8. A dislocation wall in the sample $\text{Cr}_{0.92}\text{Al}_{0.08}\text{N}$ (dotted line) that is perpendicular to the diffraction vector $\vec{q} = (2\bar{2}0)$. The micrograph was taken in the two-beam diffraction condition.

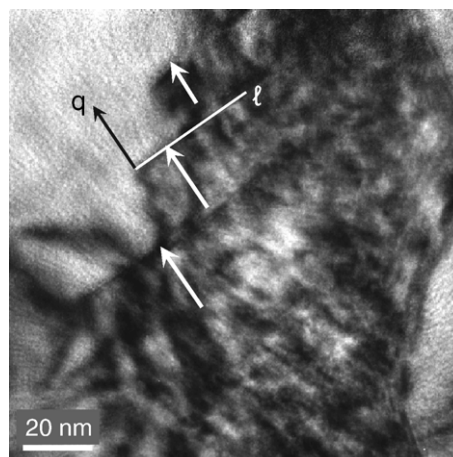


Fig. 9. A micrograph of three dislocation walls (marked by white arrows) taken at the diffraction vector $\vec{q} = (\bar{2}42)$ in the sample $\text{Cr}_{0.92}\text{Al}_{0.08}\text{N}$. $\vec{\ell} = 1/\sqrt{2}(101)$ is a unit vector lying parallel to the tilt axis of the crystallites disorientation (marked by the white line).

vector $a/2 \langle 110 \rangle$, Eq. (4) can be rewritten into the following form:

$$|\vec{b}| = a \frac{\sqrt{2}}{2} = 2|\vec{r} \times \vec{\ell}| \sin \frac{\alpha}{2} \quad (5)$$

where \vec{b} is the Burgers vector of the complete screw dislocation and a the lattice parameter. According to Eq. (4), \vec{r} has the meaning of the distance between the screw dislocations in the dislocation wall; $|\vec{r} \times \vec{\ell}|$ stands for the projection of the distance between dislocations into the imaging plane of TEM. The disorientation of crystallites due to the screw dislocations is approximately 0.75° as calculated using Eq. (5) for $|\vec{r} \times \vec{\ell}| \cong 22$ nm, which was the visible distance between the dislocations in the sample $\text{Cr}_{0.92}\text{Al}_{0.08}\text{N}$ (see Fig. 9), and for $a = 0.4145$ nm (see Fig. 3). This disorientation of crystallites is of the same order of magnitude like the disorientation of crystallites obtained from the XRD line broadening, which was 0.54° (see Fig. 6).

4. Summary and discussion

Nanocrystalline clusters were observed in all $\text{Cr}_{1-x}\text{Al}_x\text{N}$ and $\text{Cr}_{-x-y}\text{Al}_x\text{Si}_y\text{N}$ coatings under study. The crystallite size decreased with increasing aluminium and silicon contents from ~ 11 nm to ~ 4 nm. The decrease of the size of crystallites was accompanied by an increase of their mutual disorientation from 0.5° to several degrees. In the coatings without silicon ($\text{Cr}_{-x}\text{Al}_x\text{N}$), generally larger crystallites with a smaller mutual disorientation were observed than in the coatings containing silicon ($\text{Cr}_{-x-y}\text{Al}_x\text{Si}_y\text{N}$). A rapid decrease of the crystallite size was observed in the sample $\text{Cr}_{0.46}\text{Al}_{0.54}\text{N}$, in which wurtzitic AlN was found together with fcc (Cr, Al) N. In the coatings with silicon, the decrease of the crystallite size with increasing aluminium and silicon contents was faster than in the Cr–Al–N coatings. However, no rapid change of the crystallite size was observed in the sample $\text{Cr}_{0.40}\text{Al}_{0.52}\text{Si}_{0.08}\text{N}$, in which fcc-(Cr, Al)

N and wurtzitic AlN were observed concurrently. On the contrary, the mutual disorientation of crystallites increased rapidly with increasing aluminium and silicon contents in aluminium- and silicon-rich samples starting with the last “single-phase” sample $\text{Cr}_{0.52}\text{Al}_{0.43}\text{Si}_{0.05}\text{N}$. In the sample $\text{Cr}_{0.40}\text{Al}_{0.52}\text{Si}_{0.08}\text{N}$, the disorientation of crystallites exceeded the maximum disorientation, for which the phenomenon of the partial coherence of crystallites still can be observed. Thus, the disorientation of crystallites could not be calculated from the XRD line broadening; it could only be estimated to be larger than 1.4° . A similar effect was observed in the Ti–Al–Si–N coatings [31], where the loss of the crystallographic coherence of crystallites was explained by the development of amorphous Si_3N_4 between individual crystallites, which obstructed transfer of the preferred orientation between neighbouring crystallites.

The results of microstructure analysis indicated a substantial difference in the development of nanocrystallites in the Cr–Al–N and Cr–Al–Si–N coatings containing a single phase or several phases. Development of nanocrystallites in coatings containing more phases resulted from segregation of aluminium and silicon from the host structure of the fcc $\text{Cr}_{1-x-y}\text{Al}_x\text{Si}_y\text{N}$. Segregated aluminium builds nanocrystalline wurtzitic AlN, which splits fcc nanocrystallites without disturbing their partial coherence. A very strong local preferred orientation of fcc nanocrystallites with the size between 4 and 11 nm in clusters having the size between 36 and 56 nm, which is a requirement for the partial coherence of the nanocrystallites, supports the hypothesis that the nanocrystallites originate from the clusters in a decomposition process probably during the deposition process. Analogous microstructure models were discussed in numerous works, e.g. in Refs. [6,14,15,20,29–31,34,36,59–62].

The development of nanocrystallites in single-phase coatings can be illustrated on the sample $\text{Cr}_{0.92}\text{Al}_{0.08}\text{N}$. In this sample, XRD detected partially coherent nanocrystallites with the size of approximately 11 nm and with the average mutual disorientation of 0.54° . These nanocrystallites built clusters having the size of (36 ± 10) nm as obtained from XRD line broadening and confirmed by HRTEM. Using TEM, dislocation walls were found in this sample that consisted of screw dislocations with the Burgers vector $a/2 \langle 110 \rangle$, which had a distance larger than 22 nm. Assuming the above disorientation of crystallites (0.54°), the above Burgers vector of the screw dislocations ($a/2 \langle 110 \rangle$) and the vectors \vec{r} and $\vec{\ell}$ being perpendicular to each other, Eq. (5) yielded the distance between dislocations of 36 nm, which matches well with the mean size of the clusters in this particular sample. The last assumption that the vectors \vec{r} and $\vec{\ell}$ are perpendicular to each other means that the distance between dislocations is the real distance, no projection. It seems that each cluster contains typically a single screw dislocation. An issue for discussion is still the meaning of the individual partially coherent nanocrystallites, which build the nano-sized clusters. According to the experimental results, the partially coherent nanocrystallites are dislocation-free parts of the clusters that are mutually disoriented by the screw dislocations. As shown for instance in Refs. [53–55], XRD can only see the relatively undistorted core of the clusters, not the neighbourhood of dislocations or dislocation walls having an extremely high density

of microstructural defects. Therefore, the width of the regions that are strongly affected by the strain field of dislocations could be estimated from the difference between the cluster size and the sum of the crystallite sizes within individual clusters. For screw dislocations that are ideally located in the middle of the clusters, the total size of nanocrystallites per cluster would be equal to the double crystallite size. For the sample $\text{Cr}_{0.92}\text{Al}_{0.08}\text{N}$, the double crystallite size is equal to 22 nm, the size of the clusters 36 nm, thus the width of the regions that are strongly affected by the strain field of such dislocations is nearly 15 nm.

5. Conclusions

Microstructure analysis on Cr–Al–N and Cr–Al–Si–N coatings deposited using cathodic arc evaporation revealed information on their phase composition, stress-free lattice parameters, size of partially coherent nanocrystallites, their mutual disorientation in nano-sized clusters and the size of these clusters in dependence on the overall chemical composition of the coatings. In the Cr–Al–N system, a single fcc phase was stable between CrN and $\text{Cr}_{0.54}\text{Al}_{0.46}\text{N}$. Segregation of aluminium from the host structure of the fcc $\text{Cr}_{1-x}\text{Al}_x\text{N}$, which was accompanied by development of the hexagonal AlN, was observed at higher aluminium contents than $\text{Cr}_{0.54}\text{Al}_{0.46}\text{N}$. In the Cr–Al–Si–N system, the single fcc phase was stable between CrN and $\text{Cr}_{0.52}\text{Al}_{0.43}\text{Si}_{0.05}\text{N}$. At higher aluminium and silicon contents, aluminium and silicon escaped from $\text{Cr}_{1-x-y}\text{Al}_x\text{Si}_y\text{N}$. Consequently, hexagonal AlN and an amorphous phase were found. In the single-phase region, the stress-free lattice parameters were described by the function $a = [0.41486(2) - 0.00827(1) \cdot x + 0.034(1) \cdot y]$ nm, where x and y are the stoichiometric ratios of Al and Si in $\text{Cr}_{1-x-y}\text{Al}_x\text{Si}_y\text{N}$. Additional microstructural parameters were determined from the combination of XRD line broadening and TEM/HRTEM: the size of defect-free nanocrystallites, the mutual disorientation of partially coherent nanocrystallites, the size of clusters that are composed from partially coherent nanocrystallites, and the kind and distances of microstructural defects that split the clusters into the nanocrystallites.

Acknowledgements

The authors appreciate the financial support of the project # RA-1050/9 through the German Scientific Council (DFG). HRTEM Jeol 2010 FEF was purchased from the funds of the DFG Priority Programme # 1062.

References

- [1] E. Spain, J.C. Avelar-Batista, M. Letch, J. Housden, B. Lerga, Surf. Coat. Technol. 200 (2005) 1507.
- [2] C. Brecher, G. Spachtholz, K. Bobzin, E. Lugscheider, O. Knotek, M. Maes, Surf. Coat. Technol. 200 (2005) 1738.
- [3] H. Scheerer, T.H. Hoche, E. Broszeit, B. Schramm, E. Abele, C. Berger, Surf. Coat. Technol. 200 (2005) 203.
- [4] A. Sugishima, H. Kajioaka, Y. Makino, Surf. Coat. Technol. 97 (1997) 590.
- [5] Y. Makino, K. Nogi, Surf. Coat. Technol. 98 (1998) 1008.
- [6] Y. Makino, Surf. Coat. Technol. 193 (2005) 185.
- [7] D. Rafaja, M. Dopita, M. Růžička, V. Klemm, D. Heger, G. Schreiber, M. Šima, Surf. Coat. Technol. 201 (2006) 2835.

- [8] P.H. Mayrhofer, H. Willmann, C. Mitterer, Surf. Coat. Technol. 146–147 (2001) 222.
- [9] O. Banakh, P.E. Schmid, R. Sanjinés, F. Lévy, Surf. Coat. Technol. 163–164 (2003) 57.
- [10] M. Kawate, A.K. Hashimoto, T. Suzuki, Surf. Coat. Technol. 165 (2003) 163.
- [11] A.E. Reiter, V.H. Derflinger, B. Hanselmann, T. Bachmann, B. Sartory, Surf. Coat. Technol. 200 (2005) 2114.
- [12] S.R. Pulugurtha, D.G. Bhat, Surf. Coat. Technol. 201 (2006) 4411.
- [13] S. Veprek, S. Reiprich, Thin Solid Films 268 (1995) 64.
- [14] S. Veprek, A.S. Argon, Surf. Coat. Technol. 146147 (2001) 175.
- [15] S. Veprek, M.G.J. Veprek-Heijman, Surf. Coat. Technol. 201 (2007) 6064.
- [16] S. Veprek, A.S. Argon, J. Vac. Sci. Technol., B 20 (2002) 650.
- [17] J. Musil, Surf. Coat. Technol. 125 (2000) 322.
- [18] H.S. Myung, H.M. Lee, L.R. Shaginyan, J.G. Han, Surf. Coat. Technol. 163–164 (2003) 591.
- [19] P.H. Mayrhofer, G. Tischler, C. Mitterer, Surf. Coat. Technol. 142–144 (2001) 78.
- [20] I.-W. Park, D.S. Kang, J.J. Moore, S.C. Kwon, J.J. Rha, K.H. Kim, Surf. Coat. Technol. 201 (2006) 5223.
- [21] S. Veprek, J. Vac. Sci. Technol., A, Vac. Surf. Films 17 (1999) 2401.
- [22] A. Hörling, J. Sjöln, L. Karlsson, M. Odén, L. Hultman, J. Vac. Sci. Technol., A, Vac. Surf. Films 20 (2002) 1815.
- [23] P.H. Mayrhofer, A. Hörling, L. Karlsson, J. Sjöln, T. Larsson, C. Mitterer, L. Hultman, Appl. Phys. Lett. 83 (10) (2003) 2049.
- [24] M. Parlinska-Wojtan, A. Karimi, O. Coddet, T. Cselle, M. Morstein, Surf. Coat. Technol. 188–189 (2004) 344.
- [25] S. Veprek, H.D. Männling, M. Jílek, P. Holubář, Mater. Sci. Eng., A Struct. Mater.: Prop. Microstruct. Process. 366 (2004) 202.
- [26] D. Rafaja, M. Šíma, V. Klemm, G. Schreiber, D. Heger, L. Havela, R. Kužel, J. Alloys Compd. 378 (2004) 107.
- [27] P.H. Mayrhofer, H. Clemens, C. Mitterer, Z. Met.kd. 96 (2005) 468.
- [28] A. Hörling, L. Hultman, M. Odén, J. Sjöln, L. Karlsson, Surf. Coat. Technol. 191 (2005) 384.
- [29] S. Hao, B. Delley, C. Stampfl, Phys. Rev. B 74 (2006) 035402.
- [30] S. Hao, B. Delley, C. Stampfl, Phys. Rev. B 74 (2006) 035424.
- [31] D. Rafaja, A. Poklad, V. Klemm, G. Schreiber, D. Heger, M. Šíma, M. Dopita, Thin Solid Films 514 (2006) 240.
- [32] D. Rafaja, V. Klemm, G. Schreiber, M. Knapp, R. Kužel, J. Appl. Crystallogr. 37 (2004) 613.
- [33] D. Rafaja, V. Klemm, M. Dopita: Practical aspects of partial coherence of nanocrystalline domains, CPD Newsletter 34 (2006), Commission on Powder Diffraction, International Union of Crystallography, <http://www.mpi-stuttgart.mpg.de/cpd/html/newsletter.html>, in press.
- [34] D. Mercs, N. Bonasso, S. Naamane, J.-M. Bordes, C. Coddet, Surf. Coat. Technol. 200 (2005) 403.
- [35] P.H. Mayrhofer, C. Mitterer, L. Hultman, H. Clemens, Prog. Mater. Sci. 51 (2006) 1032.
- [36] P.H. Mayrhofer, D. Music, J.M. Schneider, J. Appl. Phys. 100 (2006) 094906.
- [37] J. Neidhardt, Z. Czigany, B. Sartory, R. Tessadri, M. O'Sullivan, C. Mitterer, Acta Mater. 54 (2006) 4193.
- [38] J. Neidhardt, M. O'Sullivan, A.E. Reiter, W. Rechberger, W. Grogger, C. Mitterer, Surf. Coat. Technol. 201 (2006) 2553.
- [39] P. Holubář, M. Jílek, M. Šíma, Surf. Coat. Technol. 133–134 (2000) 145.
- [40] D. Rafaja, A. Poklad, G. Schreiber, V. Klemm, D. Heger, M. Šíma, Z. Met.kd. 96 (2005) 736.
- [41] W. Mayr, W. Lengauer, P. Ettmayer, D. Rafaja, J. Bauer, M. Bohn, J. Phase Equilib. 20 (1) (1999) 35.
- [42] C.S. Sandu, R. Sanjinés, M. Benkahoul, F. Medjani, F. Lévy, Surf. Coat. Technol. 201 (2006) 4083.
- [43] W.C. Oliver, G.M. Pharr, J. Mater. Res. 7 (4) (1992) 1564.
- [44] J. Musil, F. Kunc, H. Zeman, H. Poláková, Surf. Coat. Technol. 154 (2002) 304.
- [45] A. Reuss, Z. Angew. Math. Mech. 9 (1929) 49.
- [46] H. Neerfeld, Mitt. Kaiser-Wilhelm-Inst. Eisenforsch. Düsseld. 24 (1942) 61.
- [47] E. Kröner, Z. Phys. 151 (1958) 504.
- [48] R.W. Vook, F. Witt, J. Appl. Phys. 36 (1965) 2169.
- [49] See, e.g., I.C. Noyan, J.B. Cohen: Residual stresses, measurement by diffraction and interpretation, Springer, New York, 1987.
- [50] Inorganic Crystal Structure Database, ICSD on CD-ROM, Version 1.4.1, FIZ Karlsruhe, 2006.
- [51] G.K. Williamson, W.H. Hall, Acta Metall. 1 (1953) 22.
- [52] See, e.g., M.A. Krivoglaz, X-ray and neutron diffraction in nonideal crystals, Springer, Berlin, Heidelberg, 1996.
- [53] H. Mughrabi, Acta Metall. 31 (1983) 1367.
- [54] R.E. Bolmaro, H.G. Brokmeier, J.W. Signorelli, A. Fournz, M.A. Bertinetti, in: E.J. Mittemeijer, P. Scardi (Eds.), Diffraction Analysis of the Microstructure of Materials, Springer, Berlin, 2004, p. 391.
- [55] T. Ungár, G. Tichy, J. Gubicza, R.J. Hellmig, Powder Diffr. 20 (2005) 366.
- [56] F.C. Frank, Report on the Symposium on Plastic Deformation of Crystalline Solids, Carnegie Institute of Technology and Office of Naval Research, U.S. Government Printing Office, Washington, 1950, p. 150.
- [57] See, e.g., G. Gottstein, Physical foundations of materials science, Springer, Berlin, Heidelberg, 2004.
- [58] D.B. Williams, C.B. Carter, Transmission Electron Microscopy III — Imaging, Plenum Press, New York, 1996.
- [59] P.H. Mayrhofer, D. Music, J.M. Schneider, Appl. Phys. Lett. 88 (2006) 071922.
- [60] K. Ichijo, H. Hasegawa, T. Suzuki, Surf. Coat. Technol. 201 (2007) 5477.
- [61] H. Willmann, P.H. Mayrhofer, P.O.Å. Persson, A.E. Reiter, L. Hultman, C. Mitterer, Scripta Mater. 54 (2006) 1847.
- [62] K. Yamamoto, S. Kujime, K. Takahara, Surf. Coat. Technol. 200 (2005) 1383.